Journal of Nuclear Materials 477 (2016) 149–156

Contents lists available at ScienceDirect

Journal of Nuclear Materials

journal homepage: www.elsevier.com/locate/jnucmat

α-Phase transformation kinetics of U − 8 wt% Mo established by in situ neutron diffraction

M.A. Steiner [a, *], C.A. Calhoun [a], R.W. Klein [a], K. An [b], E. Garlea [c], S.R. Agnew [a]

[a] University of Virginia, Material Science and Engineering, 395 McCormick Rd, Charlottesville, VA 22904, USA
[b] Chemical and Engineering Materials Division, Spallation Neutron Source, Oak Ridge National Laboratory, Oak Ridge, TN 37831, USA
[c] Y-12 National Security Complex, Oak Ridge, TN 37831, USA

GRAPHICAL ABSTRACT

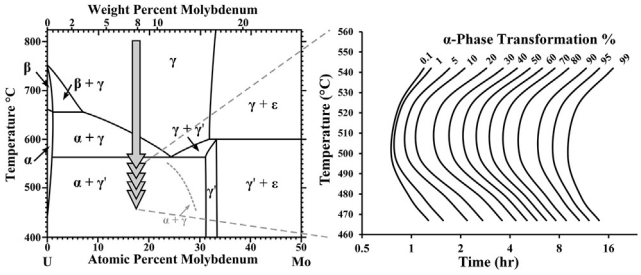

ARTICLE INFO

Article history:
Received 28 December 2015
Received in revised form
5 May 2016
Accepted 6 May 2016
Available online 8 May 2016

Keywords:
U-Mo alloys
Neutron diffraction
Time-temperature-transformation diagram
Transformation kinetics
Eutectoid decomposition

ABSTRACT

The α-phase transformation kinetics of as-cast U - 8 wt% Mo below the eutectoid temperature have been established by in situ neutron diffraction. α-phase weight fraction data acquired through Rietveld refinement at five different isothermal hold temperatures can be modeled accurately utilizing a simple Johnson-Mehl-Avrami-Kolmogorov impingement-based theory, and the results are validated by a corresponding evolution in the γ-phase lattice parameter during transformation that follows Vegard's law. Neutron diffraction data is used to produce a detailed Time-Temperature-Transformation diagram that improves upon inconsistencies in the current literature, exhibiting a minimum transformation start time of 40 min at temperatures between 500 °C and 510 °C. The transformation kinetics of U − 8 wt% Mo can vary significantly from as-cast conditions after extensive heat treatments, due to homogenization of the typical dendritic microstructure which possesses non-negligible solute segregation.

1. Introduction

The Mo-lean portion of the U-Mo system exhibits a eutectoid decomposition below 575 °C from the high temperature body centered cubic (bcc) γ-phase into the non-cubic α and γ′ phases (Fig. 1) [1] [2]. It is often desirable to quench U-Mo alloys when cooling through the eutectoid region to preserve a metastable γ-phase at ambient temperatures, maintaining both microstructural uniformity and the more isotropic material properties associated with cubic phases. The orthorhombic α-phase is considered particularly detrimental to the mechanical stability of the alloy due to its unique anisotropic properties, notably a conspicuous negative thermal expansion coefficient along one crystallographic direction [3]. Several experimental eutectoid Time-Temperature-Transformation (TTT) diagrams of the U − 8 wt% Mo system were

* Corresponding author.
E-mail address: mas4cw@virginia.edu (M.A. Steiner).

http://dx.doi.org/10.1016/j.jnucmat.2016.05.016
0022-3115/

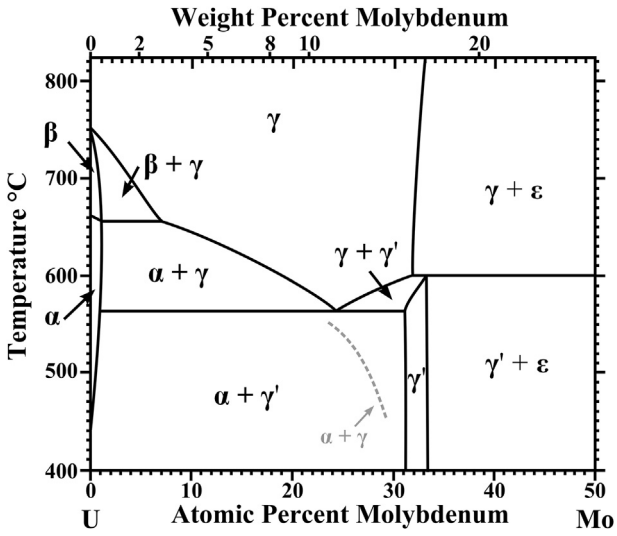

Fig. 1. Partial experimental U-Mo phase diagram in the compositional range of interest, adapted from data presented in Ref. [1]. A metastable extension of the $\alpha + \gamma$ region has been added based upon the neutron diffraction data presented in this paper.

published between 1955 and 1964, measured by a number of diverse experimental techniques including metallography, dilatometry, microhardness, x-ray diffraction, and electrical resistivity measurements [4–8]. These diagrams exhibit qualitative agreement on most of their features. The tetragonal U_2Mo intermetallic γ'-phase is much slower to form than the α-phase, and often is not detected until after the α-phase has already completed transformation. The α-phase transformation exhibits classic "nose" behavior, where the kinetics are limited at high temperatures by the smaller driving force for transformation (change in free energy), while at lower temperatures the transformation is limited by slower inter-atomic diffusion. Quantitatively, there are significant disagreements between the diagrams in regard to both the temperature of the transformation nose (510 °C ± 20 °C) and the onset of the α-phase transformation (0.4–1.9 h, nearly a factor of 5 between the extremes). The most detailed of these TTT diagrams, compiled by Repas et al. [6], combines multiple characterization techniques and places the nose at approximately 490 °C and the transformation start time at 36 min (or 0.6 h), but does not agree with any of the alternate sources.

While not to be confused with a continuous cooling transformation diagram, establishing a reliable U − 8 wt% Mo TTT diagram provides an important (though slightly conservative) estimate of the quench rate necessary to lock in the metastable cubic γ-phase at ambient temperatures. Recently, Säubert et al. have presented an in situ neutron diffraction study on the transformation of U − 8 wt% Mo including an updated TTT diagram [9]. In situ neutron diffraction offers time resolved direct quantitative phase characterization of a large volume of bulk material, and is particularly well suited to U-Mo alloys as solute partitioning results in length changes during dilatometry that cannot be deconvoluted [10]. This new diagram has significantly slower transformation kinetics than that presented by Repas, adding further uncertainty to the true location of the U − 8 wt% Mo transformation nose. It will be shown that this disagreement likely arises from microstructural differences between the as-cast state and samples that have undergone long heat treatments to fully homogenize any compositional gradients, such as those used in the Säubert study. In situ neutron diffraction experiments on as-cast U − 8 wt% Mo exhibit considerably faster kinetics than fully homogenized material, and suggest that the transformation nose on the TTT diagram will commonly occur over a microstructurally dependent range for this alloy due to the relatively slow rate of interdiffusion.

2. Experimental procedure

Five approximately 1.2 cm long and 1.24 cm diameter cylindrical samples were cut from the same depleted U (99.8 wt% U_{238}) and 8 wt% Mo as-cast rod, which was confirmed by inductively coupled plasma atomic emission spectroscopy to have a homogeneous average solute distribution across its length (7.95–7.98 wt%). Analysis shows that all trace metals are below 25 μg/g with the exception of erbium (~200 μg/g). The carbon impurity content is unknown. These samples were tested independently on the VULCAN neutron beamline at the Spallation Neutron Source located within the Oak Ridge National Laboratory [11]. Each sample, starting from the as-cast condition, was heated from ambient temperature to above 800 °C in vacuum for approximately fifteen minutes, before being cooled (10 °C/min) to an isothermal hold temperature (467 °C, 478 °C, 498 °C, 523 °C, 542 °C) that was maintained for up to 12 h. Transformation time is quoted relative to the beginning of the isothermal hold, though the samples spend an additional 5–10 min below the eutectoid temperature during cooling. Time-of-flight (TOF) neutron spectra were collected continuously on two detectors (±90°) throughout the experiments with the chopper set at 20 Hz.

After acquisition, the TOF neutron spectra were binned into five minute increments and analyzed by a combination of VULCAN Data Reduction and Interactive Visualization (VDRIVE) [12] and General Structure Analysis System (GSAS) [13] software packages. A complete isothermal spectra sequence as a function of time can be seen in Fig. 2. Rietveld refinements were performed to fit lattice parameters and phase fractions from the experimental spectra at each time step, with an average $\chi^2 = 2.13$ for the fittings and all spectra within $\chi^2 < 4.00$. It was necessary to fit three phases for the Rietveld refinements, a single α-uranium phase and two cubic γ-phases, as the cubic γ-phase peaks exhibited an intensity shoulder at some conditions due to limited Mo solute diffusion. The second γ-phase employed was given a B2 (a.k.a. CsCl) partially ordered structure to prevent any impasse in the software algorithm during refinement of the same phase with two different lattice parameters. As the neutron scattering cross-section of Mo is only 35% less than

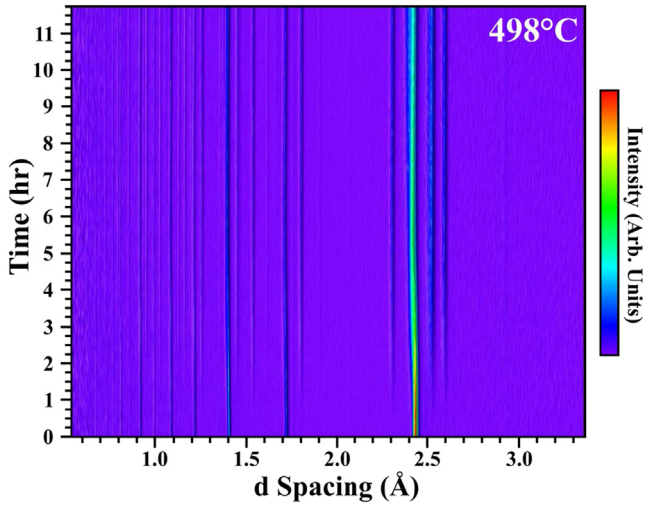

Fig. 2. Neutron diffraction spectra of U − 8 wt% Mo at 498 °C showing the transformation from $\gamma \rightarrow \gamma + \alpha$ as a function of time, with 3D shadowing effects added to enhance contrast.

U-238 [14], and Mo can only occupy only one third of the (½, ½, ½) lattice locations at this stoichiometry, the perturbation due to ordering is relatively small (the predicted superlattice peaks for the refinement do not reach above the background noise of the measurement) but the difference is enough to ensure that the second γ-phase fitting component tracked with the γ-phase peak shoulders (when present) rather than interfering with the primary γ-phase fit covering the central peaks. The γ-phase lattice parameters presented in this paper are a weighted average of these two γ-phase components. Comparison of spectra acquired on both of the detectors (±90°) confirmed that there was no preferred orientation and crystallographic texture did not influence the refinements. The data presented is exclusively from the detector bank that exhibited the highest signal to noise ratio in order to provide the best detection sensitivity for the nascent α-phase.

3. Results

Spectra from all samples exhibit peaks from only the cubic γ-phase at the start of each isothermal hold. With progressing time, peaks from the orthorhombic α-phase emerge from the background signal, and the γ-phase peaks start to develop a shoulder with a slightly smaller lattice parameter. Examples of neutron diffraction spectra at both the start and end of an isothermal hold can be found in Fig. 3, with the peak locations associated with the γ and α phases noted for reference. The shoulder, most apparent on the {110} diffraction peak due to its high intensity, appears in conjunction with the α-phase transformation and is attributed to compositional variations within the γ-phase. The eutectoid transformation of the γ-phase in U-Mo proceeds in this temperature range by a cellular reaction, producing lamellar colonies of $\alpha + \gamma$ [6] [15]. For the U − 8 wt% Mo hypo-eutectoid composition, these colonies will eventually stop growing and come into a kinetically arrested metastable thermodynamic equilibrium with the remaining γ-phase grains [6] [16] [17], after which the γ-phase in both the γ-phase grains and lamellar colonies will proceed to slowly form the γ′-phase. As the α-phase has a low (1 at%) solubility for Mo atoms, the surrounding γ-phase will enrich in Mo during transformation, especially the γ-phase portion of the lamellar colonies. Compositional variations, particularly between the lamellar and non-lamellar regions, can arise in the γ-phase due to the limited time available for diffusion of Mo away from the cellular reaction front (at 467 °C the inter-diffusion length over one hour is less than 100 nm [18] [19]). The lattice parameter of the γ-phase decreases with increasing Mo content (discussed later in this section) and this compositional variation within the microstructure explains the presence of shoulders on the γ-phase diffraction peaks. The relative intensities of these shoulders decrease progressively with higher isothermal hold temperatures and they are absent in the 542 °C spectra, consistent with the increasing rates of inter-diffusion. As the major γ-phase peak moves to smaller lattice parameters steadily along with the shoulder, much of the Mo concentration is still accommodated by bulk diffusion and does not reside solely in localized Mo-rich regions between the α-phase lamellae.

The weight fraction of α-phase, as calculated by Rietveld refinement, is plotted in Fig. 4 as a function of time for each of the isothermal conditions. The refinement software has difficulty accurately determining the α-phase weight fraction when the α-phase is first emerging from the background. This is attributed to the large number of diffraction peaks associated with interplanar spacings below 1.25 Å in the orthorhombic phase, which the refinement will attempt to spuriously fit to variations in the experimental noise. As a result, spectra without the presence of the most prominent α-phase peaks will still return 2–6 wt% fittings depending on the level of experimental background, and data below 5–9 wt% (3 wt% above the respective background fittings) has been omitted from analysis. It is clear that U − 8 wt% Mo has the fastest transformation kinetics at 498 °C of the temperatures measured, and the kinetics become slower with lower or higher isothermal temperatures. The α-phase weight fraction at transformation completion to the metastable $\alpha + \gamma$ state also varies with hold temperature, which is consistent with a metastable extension of the $\alpha + \gamma$ phase boundary (Fig. 1) and application of the lever rule to determine phase fractions.

Johnson-Mehl-Avrami-Kolmogorov (JMAK) theory [20–24], a

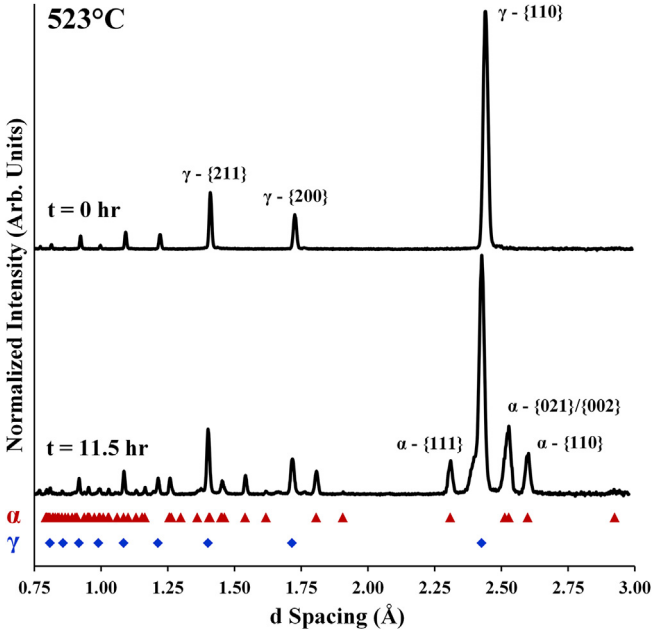

Fig. 3. Neutron diffraction spectra of U − 8 wt% Mo at 523 °C at $t = 0$ h and $t = 11.5$ h, showing the locations of the γ-phase and α-phase peaks. The intensities of both spectra are normalized to the height of the γ-{110} peak. Along with the presence of the α-phase, a shoulder on the lower d spacing side of the γ-phase peaks is apparent at this temperature (best seen on left side of the γ-{110} peak) with increasing time, highlighting compositional variations that arise within the γ-phase.

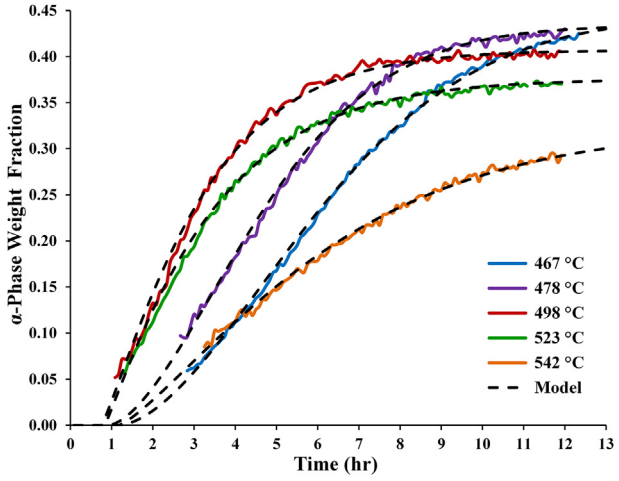

Fig. 4. The weight fraction of α-phase, as calculate by Rietveld refinement of the neutron spectra, plotted as a function of time for each of the isothermal conditions. Dashed lines represent the fit of a JMAK model to the transformation, with an $R^2 = 0.994$.

first-order model for transformations where growing regions impinge upon each other, does an excellent job at fitting the experimental α-phase weight fraction data. Changes in the α-phase weight fraction emanate from nucleation and growth of lamellar α + γ regions. Early in the transformation process the lamellar regions are isolated from each other and free to expand. As more of the volume transforms, regions begin to impinge upon each other and less untransformed volume is available for growth. For the hypo-eutectoid U - 8 wt% Mo composition, this will occur largely through "soft" impingement, where the regions are not physically impinging but instead their diffusional zones must compete. It has been shown elsewhere [24] that for all isothermal cases that follow the JMAK model, the state of transformation completion, $X\,(0 \rightarrow 1)$, can be represented by a simplified function of the form

$$X = 1 - \exp|-\kappa\, t^n| \tag{1}$$

where κ and n are temperature dependent kinetic rate constants. In order to fit this model to the data in Fig. 4, two scaling constants must also be introduced to convert between coordinate systems.

$$\alpha\ (wt\%) = F_\alpha\left(1 - \exp\left| - \kappa\left(t - t_{(X=0)}\right)^n\right|\right) \tag{2}$$

The first of these, F_α, represents the weight fraction of the α-phase at completion ($X = 1$) and scales the y-axis, and the second is the start time of the transformation, $t_{(X\,=\,0)}$, which determines the offset along the x-axis for each curve. If the scaling constants are chosen correctly, a transformation following JMAK behavior will exhibit a linear relationship in a manipulation of Eq. (1), so that

$$ln[ln[1/(1-X)]] = ln[\kappa] + n\, ln[t] \tag{3}$$

This form of the equation allows for ready determination of the kinetic rate constants from the line slope and intercept. Choice of the transformation start time is complicated by the lack of reliable refinement data for low α-phase weight fractions and was ultimately approximated from changes in the γ-phase lattice parameter (discussed next at length). The remaining three constants were co-fitted to the Rietveld refinement data in Fig. 4, with the results displayed in Table 1. The JMAK model is able to fit the experimental data with $\overline{R^2} = 0.994$, allowing for confident extrapolation of the phase fractions toward the beginning of the transformation, as well as to longer times for the two series with the slowest kinetics (467 °C and 542 °C) that did not completely transform during the length of the experiment. While the impingement-based JMAK model does an excellent job capturing the functional form of the transformation kinetics, due to the number of competing factors encompassed by the simplified form of Eq. (1) the authors would hazard against drawing quantitative conclusions regarding diffusion, nucleation or driving forces from the fitted rate constants without further corroborating data.

Vegard's law is an empirical approximation that a linear relation exists, at constant temperature, between the lattice constant of a solid solution alloy and the concentration of its constitutive elements [25]. The lattice parameter of pure γ-phase (BCC) uranium is 3.47 Å at room temperature [26], while pure molybdenum (BCC) has a lattice parameter of 3.15 Å [27]. U − 8 wt% Mo (17.75 at %) has a room temperature lattice parameter of 3.425 Å [28], which was also confirmed by this study. The 3.425 Å lattice parameter is only marginally larger than Vegard's law (3.413 Å) applied between the two pure elements, and Vegard's law is more accurate over smaller compositional ranges. Given the available phase diagram data, it is reasonable to approximate the solubility of Mo in the α-phase to be constant at 1 at% across the temperature range of the TTT diagram measurements. With this assumption, the average Mo concentration of the γ-phase can be calculated from the α-phase weight fraction as determined by Rietveld refinement and the application of mass conservation relations. Plotting the experimentally determined lattice parameters of the γ-phase versus the average Mo concentration from the fitted refinement data (Fig. 5a), it is clear that Vegard's law holds for U-Mo in these experiments with $R^2 > 0.995$ (Table 2). The use of a weighted average for the γ-phase lattice parameters (capturing local variations in Mo concentration) is important for accurately determining this behavior as up to 20% of the γ-phase intensity can reside in the peak shoulder, and implementation of a weighted average is straightforward algebraically due to the linear relationship. Coefficients of thermal expansion for γ-phase U-Mo vary between 1×10^{-5} and

Table 1
Fitted kinetic and scaling parameters for a JMAK model (Eq. (1)) for each of the isothermal hold temperatures, modeling the α-phase transformation (weight fraction) as a function of time (units of seconds).

Temperature	Ln(κ)	n	F_α (wt%)	$t_{(X=0)}$ (min)
467 °C	−17.037	1.713	0.400	70
478 °C	−15.962	1.651	0.390	55
498 °C	−10.603	1.161	0.366	45
523 °C	−9.962	1.086	0.338	50
542 °C	−12.708	1.285	0.290	70

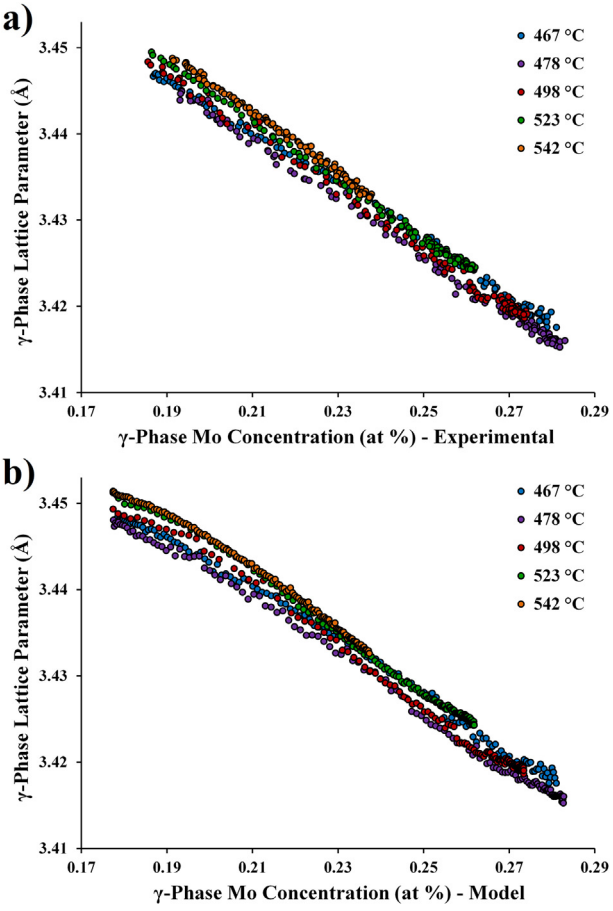

Fig. 5. a) Experimentally determined lattice parameters of the γ-phase versus the average Mo concentration calculated from the α-phase weight fraction for each of the isothermal holds, showing a clear linear relationship explained by Vegard's law. **b)** Experimentally determined lattice parameters of the γ-phase versus the average Mo concentration calculated from the JMAK model, showing a near-linear relationship including the region extrapolated by the model near the transformation start.

Table 2
Linear regressions on the lines in Fig. 5a, following Vegard's law with $R^2 > 0.995$. Variations in the slopes and intercepts are consistent with differences in thermal expansion between temperatures and concentrations (at %).

Temperature	Slope (Å/at%)	Intercept (Å)	R^2
467 °C	−0.3138	3.5060	0.9964
478 °C	−0.3304	3.5084	0.9972
498 °C	−0.3397	3.5115	0.9967
523 °C	−0.3360	3.5120	0.9981
542 °C	−0.3496	3.5159	0.9963

2×10^{-5} °C^{-1} depending on temperature and composition, with greater Mo content leading to lower coefficients of thermal expansion [29–31]. As a consequence of thermal expansion the intercepts of the lines in Fig. 5a move to larger lattice parameters with higher temperature measurements, and due the lower thermal expansion at Mo-rich concentrations the slopes in the graph steepen slightly with temperature.

Replacing the γ-phase Mo concentrations calculated directly from the fitted refinement data with those from the JMAK model (Fig. 5b), it can be seen that Vegard's law continues to hold all of the way to the transformation start (17.75 at% Mo). The lines in Fig. 5b are smoother than those in Fig. 5a, demonstrating that the JMAK model does an exceptional job at fitting the noisy refinement data, but there is some slight curvature observed in Fig. 5b, especially in the extrapolated regime below 19 at% Mo. This arises because the first-order JMAK model is unable to completely capture the kinetics of physical system (evidenced by the slight disagreements between the model and the fitted data in Fig. 4). Nonetheless, all of the curves in Fig. 5b still fit to linear regressions with $R^2 > 0.99$, confirming that despite any small discrepancies the lattice parameter data and the JMAK model are in agreement across the entire transformation, validating extrapolation of the modeled α-phase weight fractions to times near the transformation start.

The average γ-phase lattice parameter and α-phase weight fraction exhibit a clear relationship for each isothermal temperature (Fig. 6), as expected from Vegard's law. The change in lattice parameter due to increasing α-phase fraction is slow at first, when the Mo atoms expelled during formation of the α-phase are shared amongst the large balance of the alloy which exists in the γ-phase. As more α-phase forms, there is progressively less γ-phase available to share these excess Mo atoms, increasing the rate of concentration change in the γ-phase and consequently the lattice parameter. Compounding upon this, each new volume of α-phase displaces more Mo atoms than the previous due to the rising average γ-phase Mo concentration. Small variations between the curves in Fig. 6 arise from temperature dependencies in both slope and intercept of Vegard's law. Plotting changes in the γ-phase parameter as a function of time (Fig. 7) produces a graph that qualitatively resembles the fitted α-phase weight fractions in Fig. 4. The kinetics and of these curves are significantly different than that of the actual transformation, for the same reasons that all of the points in Fig. 6 do not occur along a single linear fit. Unlike the fitted α-phase weight fractions, the changes in γ-phase lattice parameter are not subject to large errors near the beginning stages of transformation, and the lattice parameters can be used to determine the approximate starting point of the phase transformation at each temperature (the $t_{(X=0)}$ parameter in Table 1).

Utilizing the verified transformation model, it is possible to construct a detailed TTT diagram across the investigated range of temperatures (Fig. 8). A spline interpolation was used to display curves between the five experimental temperatures. This diagram places the transformation nose at 40 min and somewhere between 500 °C and 510 °C. As the start of transformation could only be determined to the nearest 5 min interval, curves representing 0.1% and 1% are shown on the plot as approximate starting points. Due to the nature of the local kinetics, these two curves nearly overlap at the transformation nose and both provide a reasonable approximation of the transformation start time between 500 °C and 525 °C. Shifts in the curvature of the transformation percentile lines arise from temperature dependencies in the modeled kinetics, as well as differences in the α-phase percentile at the end of transformation. Bars representing the regions of the TTT diagram supported directly by experimental Rietveld refinement measurements have been added to the plot for reference, however experimental lattice parameter data supports interpolation of the model to all times.

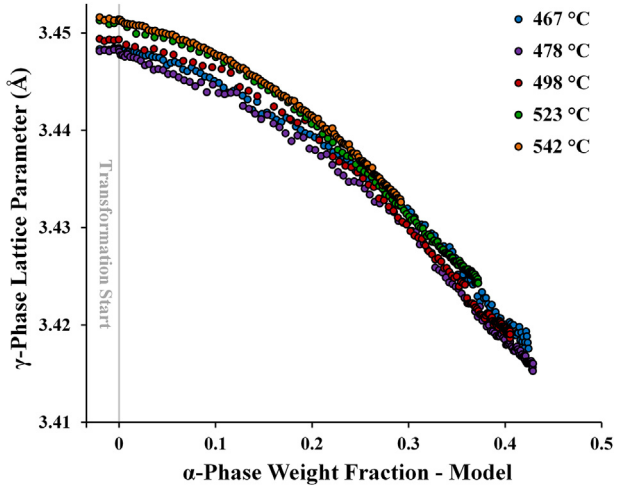

Fig. 6. The γ-phase lattice parameter plotted as a function of α-phase weight fraction for each isothermal temperature. The lattice parameter of the γ-phase, from which the α-phase transforms, decreases due to increases in Mo concentration within the diminishing fraction of γ-phase which remains to accommodate the displaced Mo from each transformed volume element. Five points before the transformation start are included as a baseline reference.

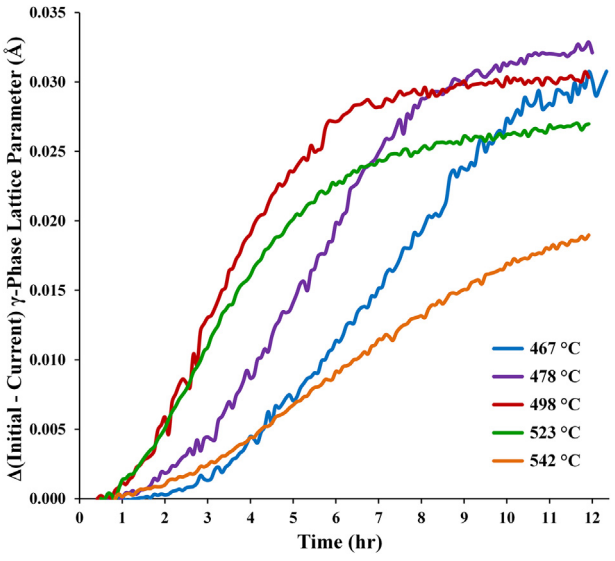

Fig. 7. Changes in the γ-phase lattice parameter plotted as a function of time for each of the isothermal conditions. These changes exhibit a similar behavior to Fig. 4 due to Vegard's law, following a relationship plotted in Fig. 6.

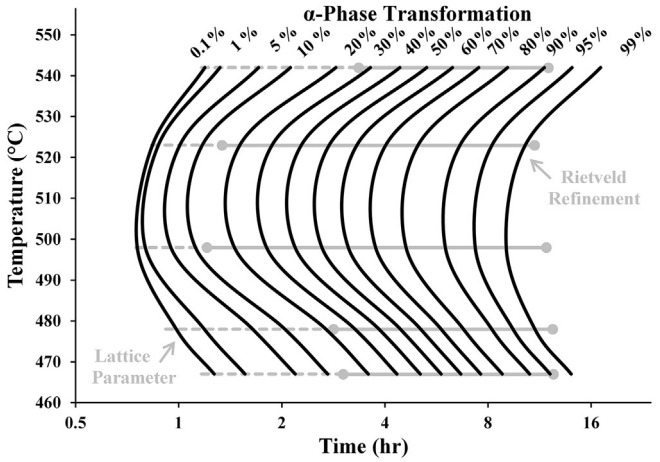

Fig. 8. Detailed TTT diagram for U – 8 wt% Mo established from neutron diffraction data. Solid bars represent instances where both experimental Rietveld refinement and lattice parameter measurements were possible, while dotted bars show data supported only by lattice parameter measurements. The curves between temperatures are spline interpolated. This diagram places the transformation nose at 40 min and somewhere between 500 °C and 510 °C.

4. Discussion

Plotting the TTT transformation start curves determined from neutron diffraction against those obtained during the 1950s and 1960s (Fig. 9) shows that there is some degree of disparity between all curves in the existing literature, especially noting that the diagram is displayed with the time axis on a log scale. Of particular concern is the lack of commonality shared by both of the recent curves determined by very similar neutron diffraction measurements [9]. The primary difference between the two neutron studies is the starting microstructural state of the samples. U-Mo alloys are prone to solute segregation during casting, forming a dendritic microstructure with Mo-rich centers [18]. Optical micrographs of the as-cast rods used in this study confirm this to be the case (Fig. 10), with an average inter-dendrite arm spacing of 24 μm.

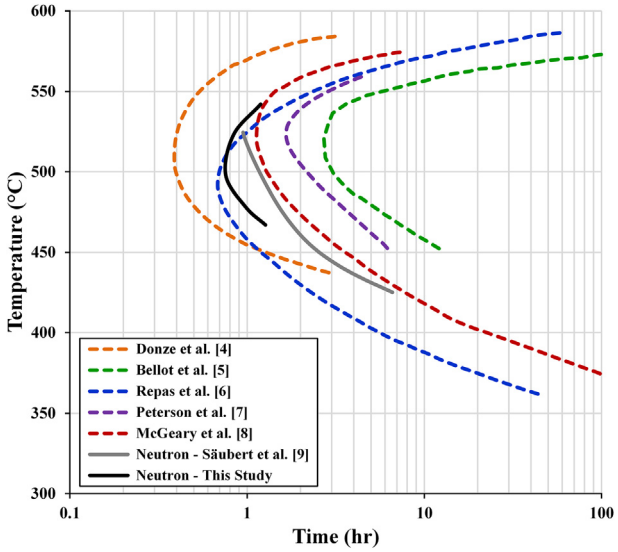

Fig. 9. U – 8 wt% Mo TTT diagrams plotting transformation start times as determined by neutron diffraction (0.1% transformed) and other sources in the literature using metallography, dilatometry, microhardness, x-ray diffraction, and electrical resistivity measurements [4–9].

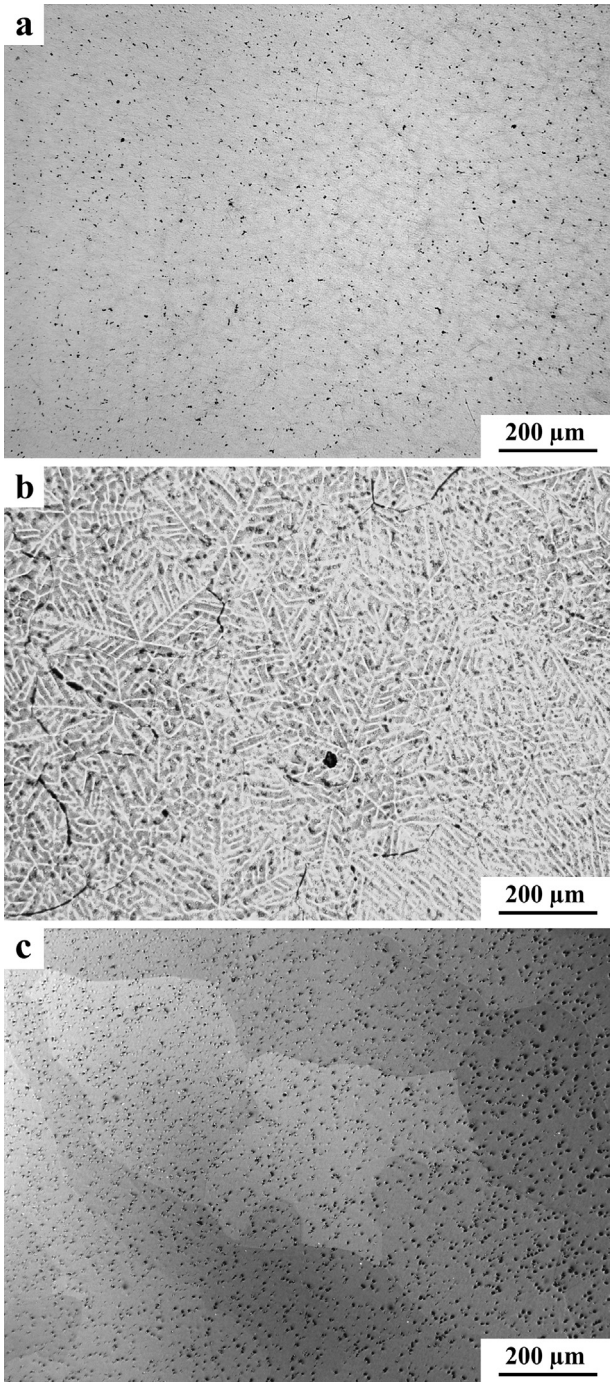

Fig. 10. **a)** Bright field optical micrograph of the as-cast U – 8 wt% Mo microstructure **b)** Bright field optical micrograph the as-cast microstructure electropolished to heighten compositional contrast in the dendritic microstructure and grain boundaries **c)** Polarized light optical micrograph of the as-cast microstructure homogenized for 24 h at 950 °C, with the polarized contrast highlighting grains of different orientations. The black specks in all three micrographs are carbon impurity based precipitates.

Based on castings which exhibit similar dendrite spacings [15], and solute segregation modeling for U-Mo alloys [18], it is expected that the composition within these dendrites varies linearly with solidified volume fraction between approximately 7 and 9 wt% Mo from edge to center. This degree of compositional variation is consistent with the breadth of the γ-phase neutron diffraction peaks and the Vegard's law relations developed previously from the peak

maxima. In contrast, the samples used in the neutron study by Säubert et al. were homogenized at 900 °C for 48 h [9], starting from a comparably sized casting expected to have a similar as-cast dendritic microstructure with commensurate levels of solute segregation. The concentration profile during homogenization of U-Mo will follow the relation [17]:

$$\Delta C = 2A \exp\left(-\frac{\pi^2 Dt}{l^2}\right) \quad (4)$$

Where ΔC is the variation in concentration starting with initial waveform amplitude A, D is the diffusion coefficient at the homogenization temperature, t is the homogenization time, and l is the inter-dendrite spacing. Homogenizing for 48 h at 900 °C ($D = 1.07 \times 10^{-14}$ m^2/s [18]) is sufficient to completely homogenize ($\Delta C/2A < 0.01$) any microstructure with an inter-dendrite spacing below 60 μm. A micrograph of one of the as-cast rods in this study that was homogenized for 950 °C ($D = 2.28 \times 10^{-14}$ m^2/s) for 24 h, a nearly identical level of homogenization to the Säubert study according to Eq. (4), is presented in Fig. 10c for comparison to the as-cast microstructure and shows that this level of heat treatment is sufficient to homogenize the small castings.

Having U − 8 wt% Mo TTT curves for both as-cast and fully homogenized microstructures is informative, as it presents two extremes for the alloy's transformation kinetics. The kinetics of U-Mo are known to slow or quicken with higher or lower Mo content, respectively [7] [8]. Compositional variation within the sample is expected to result in a leftward shift of the TTT transformation start curve relative to the fully homogenized condition, as there will be Mo lean regions (~7 wt% Mo) present between dendrites and nearest to the grain boundaries. The TTT start curve for the as-cast sample should not be confused, however, with that of homogenized U − 7 wt% Mo, as the two will experience different local diffusion gradients. The TTT transformation start curve of the as-cast samples is indeed shifted to an earlier time than the homogenized samples. The TTT curve of the homogenized samples presented by Säubert et al. is in close agreement with the earlier study of McGeary et al., which was performed on samples homogenized at 900 °C for 24 h [8], and due to this similarity it may be inferred that the curve has reached the transformation nose at 525 °C and will continue to follow the McGeary curve at higher temperatures. Interestingly, the TTT curve of the as-cast samples appears to converge closely to the Säubert/McGeary curves at temperatures above 550 °C and below 425 °C. The as-cast TTT curve corresponds best to the TTT diagram compiled by Repas et al. [6], roughly matching the transformation start time, though it underestimates the temperature of the nose by 10 °C–20 °C. The Repas study reports using samples that were homogenized at 980 °C for 4 h, but larger U-Mo castings routinely experience inter-dendrite spacings of at least 100 μm due to their slower solidification rates [32]. Consequentially, if the Repas samples were sectioned from a large casting (casting parameters were not quoted), the solute segregation profile would be largely unaffected by a short homogenization hold and the TTT curve would be similar to that determined from the as-cast samples. The large inter-dendrite spacings possible in U-Mo alloys highlights the importance of understanding both the as-cast and fully homogenized transformation kinetics of this alloy, as some degree of solute segregation is likely to remain in the microstructure in many applications. Carbon impurity levels remain a considerable unknown factor in this system warranting future study, especially as carbide impurities may serve as nucleation sites and affect transformation kinetics at early stages.

The metastable extension of the $\alpha + \gamma$ region in Fig. 1, established from the F_α parameter in this study, does not meet up with the eutectoid point of the diagram as would be expected; suggesting the eutectoid point may be located closer to 20–22 at% (9 wt%) instead of 24.5 at% [1]. The exact location of this eutectoid point has been a subject of debate between a number of phase diagram studies, all of which place it between 20 and 25 at%, but with most diagrams predicting values just short of 25 at% [1] [33]. While this deviation is not of great consequence to many applications, it is important to note the U-Mo equilibrium phase diagram is not entirely settled. The metastable extension of the $\alpha + \gamma$ region established in this paper bears an interesting correspondence to a now defunct $\alpha + \gamma'$ boundary (including the offset intersection from the eutectoid point) proposed in early work from the same authors as Ref. [1] in 1954 [34] and a separate group in 1957 [35]. Both these early studies falsely assumed that α-phase formation occurred through the production of a eutectoid lamellar microstructure of $\alpha + \gamma'$ in a cellular reaction. More recent studies [6] [30] [15], including this one, conclude that while a temperature/diffusion dependent Mo-enrichment can occur within the γ-phase lamellae, formation of the ordered γ' progresses more slowly and possibly through intermediary ordered states. It is entirely possible that the Mo-rich γ-phase in the lamellae takes the form of one of these BCC-based ordered intermediary phases (including the B2 superstructure used for the fitting), but the ordering is too weak to be determined from superlattice reflections in neutron diffraction and must ultimately be identified through methods such as transmission electron microscopy where the scattering cross sections of U and Mo have greater separation. The presence of a near-BCC ordered intermediary phase (γ'') would remove the necessity of the $\alpha + \gamma$ extension to intersect the eutectoid temperature at the eutectoid point, with the extension instead representing a $\alpha + \gamma''$ metastable region below the eutectoid.

5. Conclusions

In situ neutron diffraction can be used to establish the α-phase transformation kinetics of as-cast U − 8 wt% Mo with a high degree of accuracy. The α-phase weight fractions calculated by Rietveld refinement are shown to follow an impingement-based JMAK model function, allowing for interpolation to times approaching the transformation start where accurate refinement of the diffraction data is not possible. These results are validated for all transformation stages, including the extrapolated regimes, by changes in the γ-phase lattice parameter that closely follow Vegard's law and result from compositional shifts during formation of the α-phase. The constructed TTT diagram places the transformation nose at 40 min, located between 500 °C and 510 °C. The transformation kinetics of U − 8 wt% Mo vary significantly from as-cast conditions after extensive solution heat treatments, and for many applications the relevant TTT curve will exist between these two extremes. With the data presented in this paper the lattice parameter of γ-phase U-Mo can be accurately interpolated for other studies as a function of temperature and composition in the range of 400–600 °C and 7–15 wt% Mo. A metastable extension of the $\alpha + \gamma$ has been added to the binary phase diagram and plays an important role in alloy processing due to the significantly delayed appearance of the γ' phase, however its location raises the possibility of an error in the eutectoid point or the possibility of an intermediary ordered γ'' phase.

Acknowledgements

Funding for this research was provided by the Y-12 National Security Complex's Plant Directed Research, Development, and Demonstration program. The Spallation Neutron Source (SNS) user facility, Oak Ridge National Laboratory, is supported by the Scientific User Facilities Division, the Office of Basic Energy Sciences, the

U.S. Department of Energy. This work of authorship and those incorporated herein were prepared by Consolidated Nuclear Security, LLC (CNS) Pantex Plant/Y-12 National Security Complex as accounts of work sponsored by an agency of the United States Government under contract DE NA0001942. Neither the United States Government nor any agency thereof, nor CNS, nor any of their employees, makes any warranty, express or implied, or assumes any legal liability or responsibility to any non-governmental recipient hereof for the accuracy, completeness, use made, or usefulness of any information, apparatus, product, or process disclosed, or represents that its use would not infringe privately owned rights. Reference herein to any specific commercial product, process, or service by trade name, trademark, manufacturer, or otherwise, does not necessarily constitute or imply its endorsement, recommendation, or favoring by the United States Government or any agency or contractor thereof, or by CNS. The views and opinions of authors expressed herein do not necessarily state or reflect those of the United States Government or any agency or contractor (other than the authors) thereof. This document has been authored by Consolidated Nuclear Security, LLC, under Contract DE-NA-0001942 with the U.S. Department of Energy/National Nuclear Security Administration, or a subcontractor thereof. The United States Government retains and the publisher, by accepting the document for publication, acknowledges that the United States Government retains a nonexclusive, paid-up, irrevocable, world-wide license to publish or reproduce the published form of this document, prepare derivative works, distribute copies to the public, and perform publicly and display publicly, or allow others to do so, for U. S. Government purposes. The authors would like to thank Matt Frost of Oak Ridge National Laboratory for his logistical help throughout this experiment.

References

[1] F. Rough, A. Bauer, Constitution of Uranium and Thorium Alloys, Battelle Memorial Institute, 1958, p. 41. Vols. BMI-1300.
[2] T. Massalski, H. Okamoto, P. Subramanian, L. Kacprzak, Binary Alloy Phase Diagram, second ed., ASM International, Materials Park, OH, 1990.
[3] J.E. Burke, A.M. Turkalo, The growth of Uranium upon thermal cycling, Trans. ASM 50 (1957) 943–953.
[4] G. Donze, G. Cabane, Mécanisme de la décomposition de la phase gamma des alliages Uranium-Molybdène-Ruthénium, M. é m. Sci. Rev. Metall. LVII 6 (1960) 450.
[5] J. Bellot, P. Dosiere, J. Henry, Etude des alliages Uranium Molybdène métaux, 1958.
[6] P. Repas, R. Goodenow, R. Hehemann, Transformation Characteristics of Three Uranium Based Alloys, The Department of Metallurgy Case Institute of Technology, Cleveland, OH, 1963.
[7] N. Peterson, S. Rothman, Diffusion in gamma Uranium-, Phys. Rev. 136 (1964) 842–848.
[8] W. Bostrom, M. Burkart, E. Halteman, R. Leggett, R. McGeary, T. Padden, Development and Properties of Uranium-base Alloys Corrosion Resistance in High Temperature, Westinghouse Electric Corp. Atomic Power Div., Pittsburgh, 1955.
[9] S. Säubert, T. Zweifel, R. Jungwirth, M. Hölzel, M. Hofmann, W. Petry, Isothermal transformation kinetics in uranium molybdenum alloys, in: Transactions of the European Research Reactor Conference, 2014, pp. 48–58.
[10] S.C. Vogel, A review of neutron scattering applications to nuclear materials, ISRN Mater. Sci. 2013 (2013) 302408.
[11] K. An, H.D. Skorpenske, A.D. Stoica, D. Ma, X.L. Wang, E. Cakmak, Metall. Mater. Trans. A 42 (2011) 95.
[12] K. An, VDRIVE- Data Reduction and Interactive Visualization Software for Event Mode Neutron Diffraction, ORNL-TM-2012-621, Oak Ridge National Laboratory, 2012.
[13] A. Larson, R.V. Dreele, General Structure Analysis System, Report LAUR 86-748, Los Alamos National Laboratory, 2000.
[14] V.F. Sears, Neutron scattering lengths and cross sections, Neutron News 3 (3) (1992) 26–37.
[15] T. Pedrosa, A.D. Santos, F. Lameiras, P. Cetlin, W. Ferraz, Phase transitions during artificial ageing of segregated as-cast U–Mo alloys, J. Nucl. Mater. 457 (2015) 100–117.
[16] V.V. Joshi, E.A. Nyberg, C.A. Lavender, D. Paxton, H. Garmestani, D.E. Burkes, Thermomechanical process optimization of U-10 wt% Mo part 1: high-temperature compressive properties and microstructure, J. Nucl. Mater. 465 (2015) 805–813.
[17] V.V. Joshi, E.A. Nyberg, C.A. Lavender, D. Paxton, D.E. Burkes, Thermomechanical process optimization of U-10wt% Mo part 2: the effect of homogenization on the mechanical properties and microstructure, J. Nucl. Mater. 465 (2015) 710–718.
[18] M.A. Steiner, E. Garlea, S.R. Agnew, Modeling solute segregation during the solidification of gamma-phase U-Mo alloys, J. Nucl. Mater. 474 (2016) 105–112.
[19] K. Huang, D. Miller, Y. Sohn, Interdiffusion, intrinsic diffusion, atomicmobility, and vacancy wind effect in gamma(BCC) uranium-molybdenum alloy, Met. Trans. A 44 (2013) 738–746.
[20] W. Johnson, R. Mehl, Reaction kinetics in processes of nucleation and growth, Trans. AIME 135 (1939) 416–458.
[21] A. Kolmogorov, Izv. Akad. Nauk. SSR Ser. Fiz. Mat. Nauk. (1937) 355–360.
[22] M. Avrami, Kinetics of phase change. I general theory, J. Chem. Phys. 7 (1950) 1103–1112.
[23] C. Wert, C. Zener, Interference of growing spherical precipitate particles, J. Appl. Phys. 21 (1950) 5–8.
[24] A.T.W. Kempen, F. Sommer, E.J. Mittemeijer, Determination and interpretation of isothermal and non-isothermal transformation kinetics: the effective activation energies in terms of nucleation and growth, J. Mat. Sci. 37 (2002) 1321–1332.
[25] L. Vegard, Die Konstitution der Mischkristalle und die Raumfüllung der Atome, Z. für Phys. 5 (1) (1921) 17–26.
[26] A. Wilson, R. Rundle, The structures of uranium metal, Acta Cryst. 2 (1949) 126–127.
[27] G. Simmons, H. Wang, Single Crystal Elastic Constants and Calculated Aggregate Properties: a Handbook, 2nd. ed., MIT Press, Cambridge, MA, 1971.
[28] A.E. Dwight, The uranium-molybdenum equilibrium diagram below 900C, J. Nucl. Mater. 2 (1960) 81–87.
[29] J.M. Fackelmann, A.A. Bauer, D.P. Moak, Literature Survey on Dilute Uranium Alloys for Sandia Booster Concept, Battelle Memorial Institute, Columbus, OH, 1969.
[30] G. Beghi, Gamma Phase Uranium-molybdenum Fuel Alloys, European Atomic Energy Community, 1968. Report to the Joint Nuclear Research Center.
[31] J. Hammond, Review of Information on U-Mo Alloys and U-Mo-O2 Dispersion Fuels, Oak Ridge National Laboratory, Oak Ridge, TN, 1960.
[32] E. Nyberg, D. Paxton, V. Joshi, D. Burkes, C. Lavender, The Influence of Casting Conditions on the Microstructure of As-Cast U-10Mo Alloys: Characterization of the Casting Process Baseline, Pacific Northwest Nation Lab, 2013. PNNL-23049.
[33] A. Berche, N. Dupin, C. Guéneau, C. Rado, B. Sundman, J. Dumas, Calphad thermodynamic description of some binary systems involving U, J. Nucl. Mater. 411 (2011) 131–143.
[34] H.A. Saller, F.A. Rough, A.A. Bauer, Transformation Kinetics of Uranium-molybdenum Alloys, Battalia Memorial Institute, Columbus J Ohio, 1954. BMI-957.
[35] W. Bostrom, E. Halteman, Preprint No. 12, in: Nuclear Engineering & Science Congress (AIME), 1957.